Direct imaging of topological edge states in cold-atom systems

Nathan Goldman[a,1], Jean Dalibard[b,c], Alexandre Dauphin[a,d], Fabrice Gerbier[b], Maciej Lewenstein[e,f], Peter Zoller[g,h], and Ian B. Spielman[i]

[a]Center for Nonlinear Phenomena and Complex Systems, Université Libre de Bruxelles, B-1050 Brussels, Belgium; [b]Laboratoire Kastler Brossel, Centre National de la Recherche Scientifique, Ecole Normale Supérieure, Université Pierre et Marie Curie, 75005 Paris, France; [c]Collège de France, 75005 Paris, France; [d]Departamento de Física Teórica I, Universidad Complutense, 28040 Madrid, Spain; [e]ICFO-Institut de Ciències Fotòniques, 08860 Barcelona, Spain; [f]ICREA-Institució Catalana de Recerca i Estudis Avançats, 08010 Barcelona, Spain; [g]Institute for Quantum Optics and Quantum Information, Austrian Academy of Sciences, A-6020 Innsbruck, Austria; [h]Institute for Theoretical Physics, Innsbruck University, A-6020 Innsbruck, Austria; and [i]Joint Quantum Institute, National Institute of Standards and Technology and University of Maryland, Gaithersburg, MD 20899

Edited by Allan H. MacDonald, University of Texas at Austin, Austin, TX, and approved March 7, 2013 (received for review January 4, 2013)

Detecting topological order in cold-atom experiments is an ongoing challenge, the resolution of which offers novel perspectives on topological matter. In material systems, unambiguous signatures of topological order exist for topological insulators and quantum Hall devices. In quantum Hall systems, the quantized conductivity and the associated robust propagating edge modes—guaranteed by the existence of nontrivial topological invariants—have been observed through transport and spectroscopy measurements. Here, we show that optical-lattice-based experiments can be tailored to directly visualize the propagation of topological edge modes. Our method is rooted in the unique capability for initially shaping the atomic gas and imaging its time evolution after suddenly removing the shaping potentials. Our scheme, applicable to an assortment of atomic topological phases, provides a method for imaging the dynamics of topological edge modes, directly revealing their angular velocity and spin structure.

optical lattices | degenerate atomic gases | quantum Hall effects | chiral edge states

The integer quantum Hall (QH) effect revolutionized our understanding of quantum matter, revealing the existence of exotic phases not described by the standard theory of phase transitions (1, 2). In this phenomenon, the Hall conductivity is quantized, $\sigma_H = (e^2/h)\,\nu$—where e is the electron charge, h is Planck's constant and ν is an integer—whenever the Fermi energy resides in an energy gap. The integers ν are related to topological invariants—Chern numbers—that are associated with the bulk energy bands (1, 3, 4). Their topological origin guarantees that the Chern numbers are constant as long as the bulk gaps remain open, explaining the signature plateaus in the Hall resistivity, present when external parameters, such as magnetic fields, are varied. Moreover, a holographic principle stipulates that a topologically ordered bulk gap, with topological invariant ν, necessarily hosts ν propagating modes localized on the sample's edge (5). These topological edge states are chiral—their motion has a well-defined orientation—inhibiting scattering processes in the presence of disorder.

In condensed matter physics, direct observations of edge states remain relatively rare. A first signature was obtained from magnetoplasmons created by pulsed voltages (6). Other evidence arises from edge transport in engineered Aharonov–Bohm interferometers with QH systems (7, 8). By contrast, the "routinely used" spectroscopic reconstruction of mid-gap states (1) is consistent with the expected topological band structure but does not prove their chiral nature.

Cold atoms trapped in optical lattices and subjected to synthetic gauge fields (9, 10) are an ideal platform for realizing topological insulating phases. Making topology manifest in experiments, however, is a fundamental challenge. In this context, transport experiments are conceivable (11) but technically demanding. Existing proposals for measuring topological invariants (12–16) have experimental drawbacks and can only be applied to very specific configurations. Likewise, detecting topological edge states (17–22), for example through light-scattering methods (23), requires complicated manipulations to separate the small edge-state signal from the bulk background (20, 24).

Here, we introduce a simple method to directly visualize the propagation of topological edge modes, by studying the time evolution of an atomic QH system after suddenly releasing constraining walls (Fig. 1). We show that the movement of the chiral edge states, encircling the initially vacant regions, is directly visible in the atomic density. This reveals the edge states' angular velocity and provides an unambiguous signature of chiral edge modes in the atomic system (Fig. 1). Our method is straightforward and insensitive to experimental imperfections: It only relies on a large initial occupancy of edge states. Crucially, our method requires that the edge states contribution to the density remains spatially separated from the bulk, which can be realized by populating a dispersionless bulk band with a nonzero Chern number. We present several detection techniques, applicable to both flat and dispersive bands, that demonstrate the universal applicability to atomic systems with propagating edge modes.

We consider a two-dimensional optical lattice filled with noninteracting fermions, subjected to a uniform synthetic magnetic flux Φ (25, 26), and confined by a circular potential, $V_{\rm conf}(r) = V_0 (r/r_0)^\gamma$. In the experiment, $V_{\rm conf}(r)$ can be made nearly arbitrarily sharp ($\gamma \to \infty$) (27, 28); this configuration is of particular interest for our scheme, as demonstrated below. The resulting system realizes the Hofstadter model (29) with second-quantized Hamiltonian

$$\hat{H} = -J \sum_{m,n} \hat{c}^\dagger_{m+1,n} \hat{c}_{m,n} + e^{i2\pi\Phi m} \hat{c}^\dagger_{m,n+1} \hat{c}_{m,n} + \text{h.c.} + \sum_{m,n} V_{\rm conf}(r)\; \hat{c}^\dagger_{m,n} \hat{c}_{m,n}. \quad [1]$$

$\hat{c}^\dagger_{m,n}$ describes the creation of a fermion at lattice site $\boldsymbol{x}/a = (m,n)$, where m,n are integers; J is the tunneling amplitude; and we take the lattice period a as our unit of length. This model has a topological band structure (1, 4): When $\Phi = p/q \in \mathbb{Q}$, the bulk energy spectrum splits into q subbands (29), each associated with a nonzero Chern number (4). This guarantees the existence of robust edge states in the bulk energy gaps (5). These edge states are chiral in the sense that they propagate along the Fermi radius R_F (i.e., the edge of the atomic cloud delimited by the confining potential $V_{\rm conf}$) with a definite orientation of propagation. It is convenient to represent such nontrivial spectra by diagonalizing the Hamiltonian Eq. **1** on a cylindrical geometry (5) (Fig. 2). This picture shows a

Author contributions: N.G., J.D., F.G., M.L., P.Z., and I.B.S. designed research; N.G. and A.D. performed research; N.G. analyzed numerical data; and N.G., J.D., M.L., P.Z., and I.B.S. wrote the paper.

The authors declare no conflict of interest.

This article is a PNAS Direct Submission.

[1]To whom correspondence should be addressed. E-mail: ngoldman@ulb.ac.be.

This article contains supporting information online at www.pnas.org/lookup/suppl/doi:10.1073/pnas.1300170110/-/DCSupplemental.

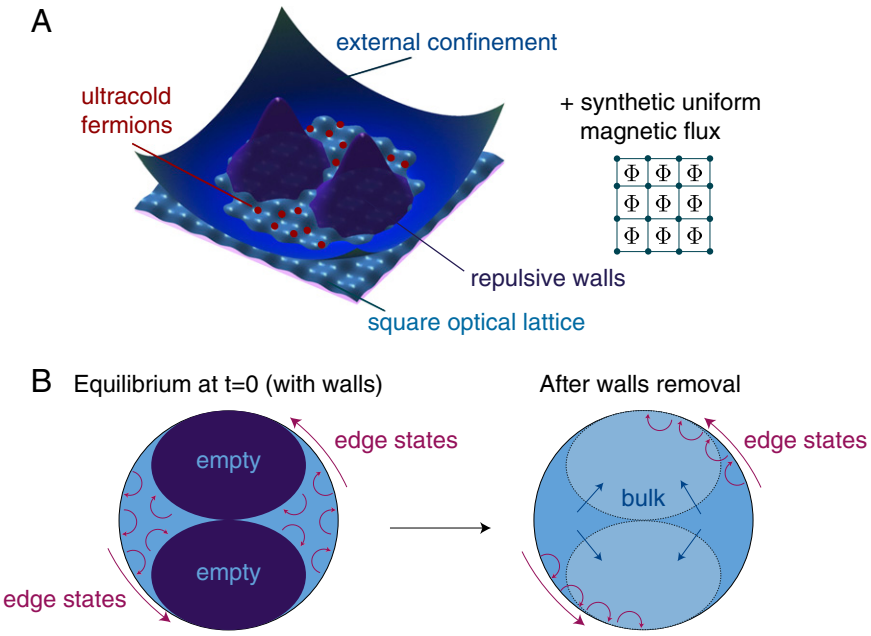

Fig. 1. Experimental scheme and general strategy. (*A*) Trapped cold atomic fermions move on a square optical lattice in the presence of a synthetic uniform magnetic flux Φ. Two repulsive potentials, initially forming holes in the atomic cloud, are suddenly removed at time $t=0$. At all times, atoms are confined by an additional circular potential. We generally assume that the confining barriers are perfectly sharp but eventually discuss the case of smoother potentials. (*B*) The system is initially prepared in a quantum Hall phase: Chiral edge states propagate along the edges determined by the repulsive walls and the external confinement. After releasing the walls, the edge states tend to propagate along the Fermi radius determined by the circular confinement: They encircle the initially vacant regions.

clear separation of the bulk and edge states dispersions that survive in the experimental circular geometry produced by $V_{\rm conf}$ (20, 24, 30). In the following, we specifically study the configurations $\Phi=1/3$ and $\Phi=1/5$ and set the Fermi energy $E_{\rm F}=-1.5J$ inside the lowest bulk energy gap (Fig. 2). In both these situations, the lowest energy band is associated with the Chern number $\nu=-1$, which guarantees the occupancy of a single edge mode with same chirality $\mathrm{sign}(\nu)=(-)$. These two configurations differ significantly in that the occupied bulk band is nearly flat (dispersionless) in the case $\Phi=1/5$, while it is dispersive for $\Phi=1/3$ (Fig. 2).

Our scheme (*i*) demonstrates the existence of propagating modes that are localized close to the Fermi radius and (*ii*) identifies their chirality and angular velocity $\dot{\theta}$. To achieve this goal, we consider a geometry that constrains the QH system within two regions of the trap, as sketched in Fig. 1, resembling a bat in flight. This initial "bat" geometry is shaped by a pair of sharp potential walls $V_{\rm hole}=V_{\rm hole1}+V_{\rm hole2}$ defined by $(x\pm r_0/2)^2+(y/\sqrt{2})^2<r_0^2/4$, creating holes in the density distribution (*SI Appendix*). In the bat geometry, we set the Fermi energy within the lowest bulk gap $E_{\rm F}=-1.5J$ and suddenly remove $V_{\rm hole}$ at time $t=0$. We then study the dynamics of the atomic density with all other parameters unchanged. The bat shape is optimized for visualizing the time-evolving chiral edge states in the density $\rho(\boldsymbol{x},t)$ for $t>0$ (Fig. 1*B*). In the following, we discuss how this "wall-removal" strategy can be exploited to reveal the edge states properties, as they progressively encircle the initially empty regions in a chiral manner.

Results

Time-Evolving Density for Dispersive Systems. Fig. 3*A* shows the time-evolving density distribution $\rho(\boldsymbol{x},t)$ for $\Phi=1/3$. This example highlights the importance of the bulk band structure, because it demonstrates the drawbacks encountered when preparing a system with dispersive bulk bands (Fig. 2*A*). The time evolution in Fig. 3*A* illustrates two main effects: (*i*) the progressive encircling of the holes by particles at the system's radial-edge (with localization length $\sim a$) and (*ii*) the undesired and rapid filling of the holes by bulk states (Fig. 1*B*). Once $t\approx 10-20\hbar/J$, the atomic cloud's initial bat shape has become cyclonic, already indicating the presence of chiral edge states. To provide further insight, we separately calculated the contribution stemming from the initially populated edge states, $\rho_{\rm edge}(\boldsymbol{x},t)$ (*Materials and Methods*). In the corresponding Fig. 3*B*, we observe that the edge states, which propagated along the edges delimited by the bat potential at $t<0$, become localized along the circular edge at $r=R_F$, and that they follow a "chiral" motion. These edge states remain localized on the edge for very long times and only slightly disperse into the bulk of the system, as can be anticipated from the small wavefunction overlap between edge and bulk states. Fig. 3*A* emphasizes the problematic (nonchiral) filling of the holes by the many dispersive bulk states, which strongly inhibits the detection of the edge states in experiments. The speed at which this filling occurs is to be compared with the circular motion of the edge states, which can be estimated from the group velocities $v=(1/\hbar)\partial E/\partial k$ associated with the bulk and edge states (Fig. 2*A*). Additional interference takes place within the system, leading to small but visible patterns in the density. Fig. 3*B* shows that these patterns mainly originate from interferences between bulk states.

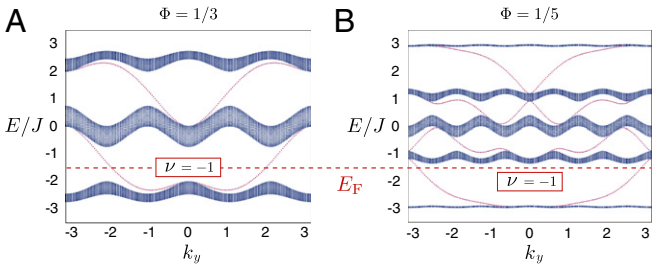

Fig. 2. Bulk and edge states spectrum: dispersive vs. flat bands. Energy spectrum $E(k_y)$ as a function of the quasi-momentum k_y for (*A*) $\Phi=1/3$ and (*B*) $\Phi=1/5$, obtained by diagonalizing the Hamiltonian Eq. **1** on a finite cylinder directed along the x direction, with $V_{\rm conf}=0$. The projected bulk bands $E(k_x,k_y)\to E(k_y)$, shown in blue, are separated by large gaps of order $\sim J$. The red dispersion branches that are visible within the bulk gaps correspond to propagating modes that are localized on the opposite edges of the cylinder. When the Fermi energy is set within the first bulk gap, a single edge mode is populated on each edge of the cylinder (the lowest bulk band corresponds to the Chern number $\nu=-1$ for $\Phi=1/q$). When considering the circular geometry realized in an experiment ($V_{\rm conf}\neq 0$) and setting $E_{\rm F}=-1.5J$, one is guaranteed that a single edge mode will be populated because the Chern number ν does not rely on the specific geometry used (20, 24, 30). When $\Phi=1/5$, the lowest energy band is characterized by the tiny flatness ratio, $f=W/\Delta\approx 0.04$, where $W(\Delta)$ denotes the first band (gap) width; in this topological quasi-flat band configuration, the populated edge states are expected to propagate more rapidly than the bulk.

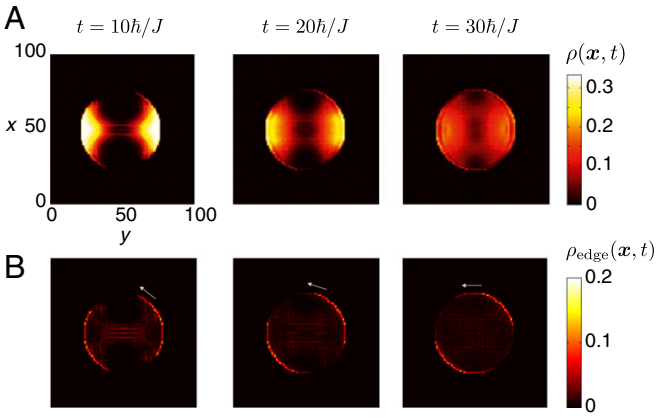

Fig. 3. Evolution of the spatial densities after releasing the walls. (*A*) The spatial density $\rho(\boldsymbol{x},t)$, and (*B*) the contribution of the initially populated edge states $\rho_{\rm edge}(\boldsymbol{x},t)$. The chiral motion is a signature of the nontrivial Chern number $\nu \neq 0$. In all the figures, $\Phi = 1/3$, $E_{\rm F} = -1.5J$, and we considered infinitely sharp circular confinement ($r_0 = 27a$) and ellipsoidal walls $V_{\rm hole}$. The total number of particles is $N_{\rm part} = 210$, whereas the number of initially populated edge states is $N_{\rm edge} \approx 80$.

Flat Topological Bulk Bands. For $\Phi = 1/5$ and $E_{\rm F} = -1.5J$, the dispersionless (flat) bulk band represented in Fig. 2*B* is totally filled, and most of the edge states lying in the first bulk gap are populated. The corresponding time-evolving density $\rho(\boldsymbol{x},t)$, depicted in Fig. 4*A*, is radically different than for $\Phi = 1/3$ (Fig. 3*A*). For $\Phi = 1/5$, the edge states encircle the initially forbidden regions in a chiral manner, largely unperturbed by the now motionless bulk, making them directly visible in in situ images of the cloud. The dispersionless nature of the bulk states is further illustrated in Fig. 4*C*, which shows the evolution of $\rho_{\rm bulk}(\boldsymbol{x},t) = \rho(\boldsymbol{x},t) - \rho_{\rm edge}(\boldsymbol{x},t)$. The initial bulk states are immobile for times $\sim 30\hbar/J$. In Fig. 4*B*, the evolution of the initially populated edge states $\rho_{\rm edge}(\boldsymbol{x},t)$ shows an interesting behavior: Some edge states with energies close to the flat bulk band are almost dispersionless and remain localized on the edges delimited by the bat potential. In contrast, the many edge states at higher energies are dispersive, encircling the holes in a clear and chiral manner. The instructive dynamics of the density $\rho(\boldsymbol{x},t)$, which is due to the clear separation of the edge and bulk states during the evolution, can also be understood by studying the population of the single-particle eigenstates (*SI Appendix*). Moreover, our method is highly robust against perturbations in the density (or equivalently in the Fermi energy, $E_{\rm F} \approx -1.5J + \delta$), because it only relies on the occupation of dispersionless bulk states and sufficiently many edge states. We verified that the edge-state signal is unambiguous when a high energy (dispersive) band is initially filled (*SI Appendix*). Thanks to the topological quasi-flat band configuration, the edge states propagation can be visualized on long time scales, without being affected by the bulk dispersion. For $\Phi = 1/5$ and a typical system size $R_F \sim 100a$, we find $\dot{\theta} \sim 0.01J/\hbar$, which would require a realistic time $t \sim 70\hbar/J$ to observe the $\pi/4$-rotation undergone by the edge states. We verified that our results are stable when the spacious ellipsoidal walls are replaced by small perturbative potentials (*SI Appendix*). Finally, the edge/bulk ratio can be further improved by initially confining the entire atomic cloud to a small region located in the vicinity of the circular edge (*SI Appendix*).

Revealing Topological Edge States in Dispersive Systems. We now describe two methods for isolating the edge-states contribution $\rho_{\rm edge}$ from that of the bulk states, useful for systems with dispersive bulk bands. The first method consists in performing two successive experiments, using the same apparatus and parameters, but with opposite fluxes Φ and $-\Phi$. The difference between the two images $\delta\rho(\boldsymbol{x},t) = \rho(\boldsymbol{x},t;+\Phi) - \rho(\boldsymbol{x},t;-\Phi)$ lacks the nonchiral contribution of the bulk states and is simply given by $\delta\rho \approx \rho_{\rm edge}(+\Phi) - \rho_{\rm edge}(-\Phi)$ (Fig. 5). For our bat geometry, $\rho_{\rm edge}(+\Phi) \approx \rho_{\rm edge}(-\Phi)$ when the edge states have undergone a rotation of $\theta = \pi/2$. This determines the time $t^* = \pi/(2\dot{\theta})$ when the signal $\delta\rho(\boldsymbol{x},t^*)$ disappears, giving the angular velocity of the edge states. This situation is illustrated in Fig. 5 for the $\Phi = 1/3$ "dispersive" case, where we find $\delta\rho(\boldsymbol{x},t^* \approx 49\hbar/J) \approx 0$, in good agreement with the angular velocity $\dot{\theta}_e \approx 0.03J/\hbar$ of the populated edge states (20, 24). We verified that slight differences in the filling [e.g., $E_{\rm F}(\Phi_+ = +1/3) \approx E_{\rm F}(\Phi_- = -1/3) \pm 0.1J$], for example due to finite temperature effects between the two successive experiments, or variations in the flux (e.g., $\Phi_+ = 1/3$ and $\Phi_- \approx -\Phi_+ \pm 0.01$), do not significantly affect the signal $\delta\rho(\boldsymbol{x},t)$, highlighting the robustness of this method against experimental imperfections.

The second method aims to efficiently reduce the bulk dispersion by suddenly lowering the potential walls $V_{\rm hole}$ at $t = 0$, instead of removing them completely. This operation can be achieved in such a way that only the edge states with sufficiently high energies are allowed to propagate, while leaving the bulk states away from the holes. This "edge-filter method" can be realized by setting the Fermi energy within the first bulk gap and then suddenly lowering the potential $V_{\rm hole}$ to the value $V_{\rm hole}^{t>0} \sim W$ at $t = 0$, where W is the width of the lowest bulk band. The great efficiency of this method is presented in *SI Appendix* for the case $\Phi = 1/3$.

Robustness of the Edge States Against Disorder. We now investigate the robustness of the edge states motion in the presence of disorder. This perturbation, which plays a fundamental role in solid-state systems, can be engineered in optical-lattice setups, for instance using speckle potentials (31). We study the effects of disorder by considering a random potential $V_{\rm rand}$, with energies uniformly distributed within the range $V_{\rm rand}(\boldsymbol{x}) \in [-D, D]$. The results are presented in Fig. 6 for the case $\Phi = 1/5$. We find that the chiral edge states signal remains robust for disorder strengths $D \lesssim 1.5J \approx \Delta$, where Δ is the size of the bulk gap. Interestingly, we can still distinguish a cyclonic cloud—a signature of the edge states chirality—for values up to $D \sim 3J \approx 2\Delta$. The immunity of

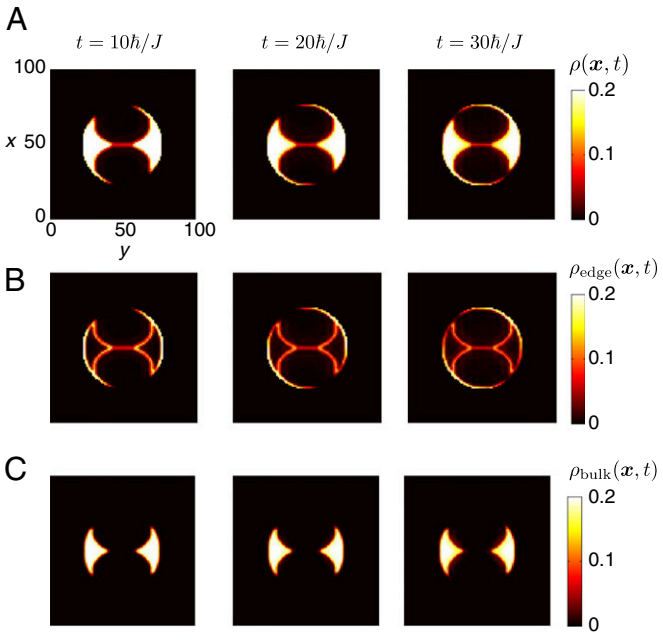

Fig. 4. The topological quasi-flat band configuration. (*A*) The spatial density $\rho(\boldsymbol{x},t)$, (*B*) the contribution of the initially populated edge states $\rho_{\rm edge}(\boldsymbol{x},t)$, and (*C*) the contribution of the initially populated bulk states $\rho_{\rm bulk}(\boldsymbol{x},t)$. In all the figures, $\Phi = 1/5$ and $E_{\rm F} = -1.5J$. The total number of particles is $N_{\rm part} = 146$, whereas the number of initially populated edge states is $N_{\rm edge} \approx 64$. Note the dispersionless nature of the occupied bulk states, which highly improves the detection of the edge-state signal.

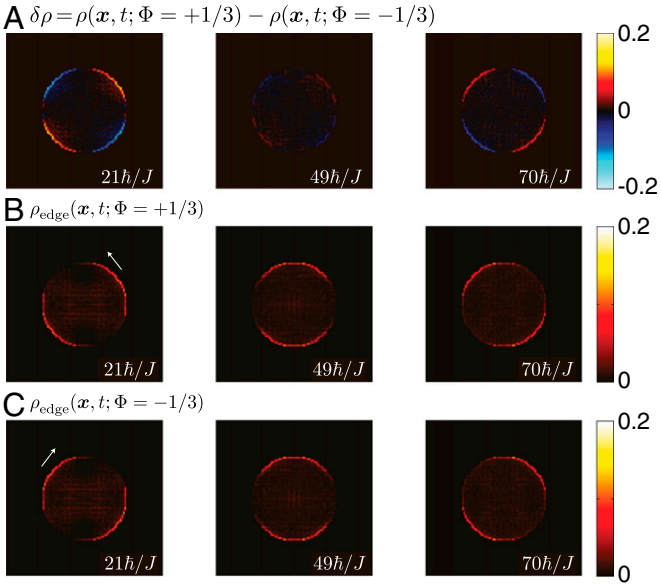

Fig. 5. The opposite-flux method for dispersive systems. (*A*) Evolution of the difference $\delta\rho=\rho(\boldsymbol{x},t;\Phi=+1/3)-\rho(\boldsymbol{x},t;\Phi=-1/3)$, for the same configuration as in Fig. 3. This method yields a clear manifestation of the edge states, $\delta\rho\approx\rho_{\rm edge}(+\Phi)-\rho_{\rm edge}(-\Phi)$, by eliminating the undesired contribution of the many bulk states. The edge states chirality is deduced from the evolution of the red and blue patterns. (*B*) The edge-states contribution $\rho_{\rm edge}(\boldsymbol{x},t)$ for $\Phi=+1/3$ and (*C*) for $\Phi=-1/3$. In the central column, we note the vanishing of the signal $\delta\rho(\boldsymbol{x})\approx 0$ that occurs at time $t^*\approx 49\hbar/J$, indicating that the edge states angular velocity is $\dot\theta\sim 0.03J/\hbar$ for $R_F=27a$ and $\gamma=\infty$ (*SI Appendix*).

the chiral edge states against disorder, a hallmark of the QH effect, could thus be demonstrated using our cold-atom setup.

Gaussian Walls and Smooth Circular Confinements. In the absence of walls $V_{\rm hole}=0$, the edge states lying in the first bulk gap are radially localized, with a radius determined by their energy and the circular confinement. Writing the circular confinement as $V_{\rm conf}(r)=V_0(r/r_0)^\gamma$, we find that an edge state ϕ_e with energy ϵ_e is characterized by a localization radius

$$R_e=r_0\sqrt[\gamma]{|\epsilon_e-\epsilon_{\rm min}|/V_0}, \qquad [2]$$

where $\epsilon_{\rm min}$ is the minimum of the bulk band. This result is illustrated in Fig. 7, for $r_0=21a$, $V_0=J$, and $\gamma=\infty,10,4$, where the wavefunctions amplitudes $|\phi_\lambda(x,y)|^2$ are plotted as a function of the x coordinate, and their corresponding energies ϵ_λ. For an infinitely abrupt trap (27), $\gamma=\infty$, all the edge states are located at the constant Fermi radius $R_{\rm F}=r_0$. Therefore, the edge states contribution to the density $\rho_{\rm edge}$ yields a clear circular signal, with localization length of the order of the lattice spacing a. In contrast, for finite γ, the populated edge states are localized on different radii $R_e\in[R_{\rm F}-\delta r,R_{\rm F}]$, leading to a broadening of the edge-state signal $\rho_{\rm edge}$. For the situation illustrated in Fig. 7, this broadening is of the order $\delta r\sim 5a$ for $\gamma=10$ and $\delta r\sim 10a$ for $\gamma=4$. Let us stress another crucial aspect of these smoothly confined QH systems, which is the fact that the angular velocity $\dot\theta$ of the chiral edge states, as well as the number $N_{\rm edge}$ of available edge states within a bulk gap, highly depend on the potential's smoothness γ: The angular velocity is maximized for highly abrupt confinements ($\gamma\to\infty$), whereas the number $N_{\rm edge}$ is larger for smooth potentials (19, 20, 24, 30). We numerically evaluated the angular velocity of the edge states (20, 24) for $\Phi=1/5$ and $r_0=21a$, and we found $\dot\theta_e\approx 0.06J/\hbar$ for $\gamma=\infty$, $\dot\theta_e\approx 0.02J/\hbar$ for $\gamma=10$, and $\dot\theta_e<0.01J/\hbar$ for $\gamma=4$ (and we note that the angular velocity $\dot\theta_e\propto 1/R_e$). Scaling to a more realistic radius $r_0=100a$, we find that the edge states, which are populated below $E_{\rm F}=-1.5J$, undergo a rotation of $\pi/5$ after a time

$$t(\theta=\pi/5)\sim 50\hbar/J, \qquad \gamma=\infty\ (r_0=100a),$$
$$t(\theta=\pi/5)\sim 150\hbar/J, \qquad \gamma=10\ (r_0=100a),$$
$$t(\theta=\pi/5)\sim 300\hbar/J, \qquad \gamma=4\ (r_0=100a),$$

indicating that it is highly desirable to design a sharp circular confining trap $\gamma\gg 10$ (27), to clearly observe the edge states rotating motion during reasonable experimental times $t\sim 10-100\hbar/J$.

We now investigate the density evolution $\rho(\boldsymbol{x},t)$ for smooth confining traps and initial Gaussian walls $V_{\rm hole}$. First of all, we note that the presence of Gaussian walls does not destroy the edge states lying within the first bulk gap. In this bat geometry, the edge states are localized on the outer edge delimited by $V_{\rm conf}(r)$, but also on the smooth boundary delimited by the Gaussian potentials. Therefore, when $\gamma\sim\infty$, the edge states behave as in Fig. 7*A* in the vicinity of the outer circular edge $r\approx r_0$, whereas they behave similarly as in Fig. 7*C* in the vicinity of the Gaussian walls. We point out that, in our scheme, it is the behavior of the edge states near the outer circular edge that plays an important role. Indeed, as shown in Fig. 8*A*, replacing the infinitely abrupt walls $V_{\rm hole}$ by Gaussian potentials does not qualitatively affect the evolution of the density $\rho(\boldsymbol{x},t)$ presented in Fig. 4*A*.

However, as can be anticipated from the discussion above, replacing the perfectly sharp potential $V_{\rm conf}(r)$ by smoother confinements, $\gamma=\infty\to 4$, has dramatic consequences on the dynamics. In Fig. 8*B*, which shows the evolution of the density for $\gamma=10$, we clearly observe the broadening $\delta r\sim 5a$ of the edge-state contribution $\rho_{\rm edge}(\boldsymbol{x},t)$, as they progressively encircle the holes. We also note the slower motion undergone by the edge states, which have a reduced angular velocity $\dot\theta(\gamma=10)\sim\dot\theta(\gamma=\infty)/3$, as seen above. An even more dramatic situation is illustrated for the case $\gamma=4$ in Fig. 8*C*. These results demonstrate the robustness of the edge-state motion in the presence of smooth confining traps and Gaussian walls, but they greatly emphasize the importance of designing sharp external confinements to improve the experimental detectability of the topological edge states.

Conclusions

In this article, we introduced a simple, yet powerful, method to image the dynamics of topological edge states in atomic systems.

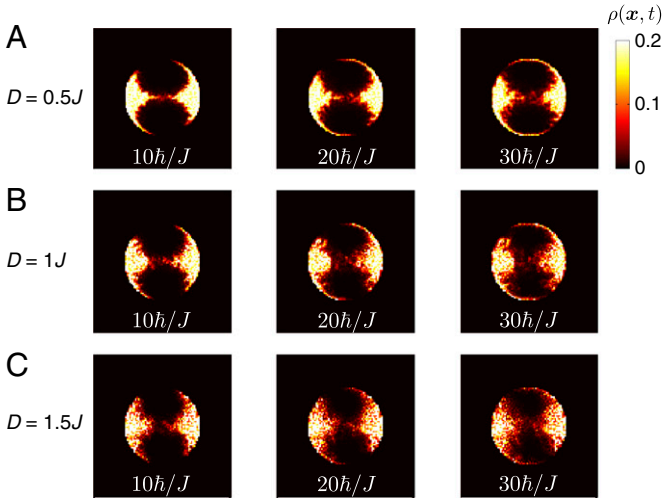

Fig. 6. Effects of disorder. The spatial density $\rho(\boldsymbol{x},t)$ for $\Phi=1/5$, $E_{\rm F}=-1.5J$, $r_0=27a$, and $\gamma=\infty$. The disorder strength is (*A*) $D=0.5J$, (*B*) $D=1J$, and (*C*) $D=1.5J$.

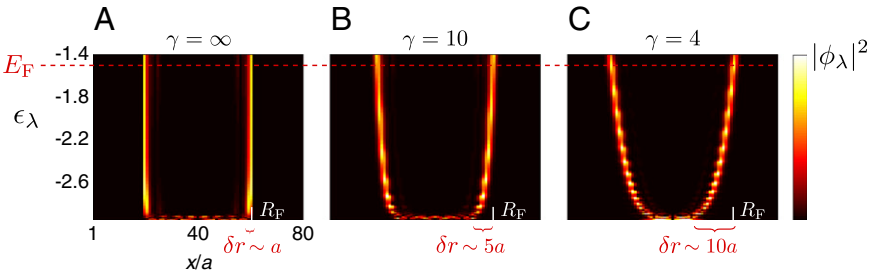

Fig. 7. Smooth confinements and edge states. The amplitudes $|\phi_\lambda(x,y)|^2$ of the single-particle wavefunctions as a function of the x coordinate and their corresponding energy ϵ_λ, and setting y at the center of the trap. Here, $\Phi=1/5$, and the external potential is given by $V_{\text{conf}}(r)=V_0(r/r_0)^\gamma$, with $r_0=21a$ and $V_0=J$. (*A*) $\gamma=\infty$, (*B*) $\gamma=10$, and (*C*) $\gamma=4$. The Fermi radius R_F is shown for $E_F=-1.5J$. The populated edge states ϕ_e are localized on the radii $R_e=R_e(\epsilon_e)$ (Eq. **2**), leading to a broadening δr of their contribution to the spatial density ρ_{edge} for finite γ.

Our scheme shapes an atomic gas, initially prepared in a topological phase, and directly images its time evolution. By explicitly revealing the presence of propagating chiral edge modes, this method provides an unambiguous signature of topological order in the context of cold atomic gases. Importantly, we have discussed the applicability of our method under realistic experimental conditions, emphasizing the importance of using sharp confining potentials to improve the detection of the edge-states signal. The schemes introduced in this work to reduce, or even eliminate, the irrelevant contribution of dispersive bulk states can be applied to a wide family of topological atomic systems, such as the promising Haldane-like optical lattice (12, 14) and fractional QH atomic gases (32–34). Finally, our method can be directly extended to visualize the propagation of Z_2 topological (spin-polarized) edge states, both in 2D (18, 35) and 3D (36), by using standard spin-dependent imaging methods (28).

Materials and Methods

The system is prepared in the ground-state of the initial Hamiltonian,

$$\hat{H}_0=\hat{H}+\sum_{m,n}V_{\text{hole}}(m,n)\,\hat{c}^\dagger_{m,n}\hat{c}_{m,n}, \qquad [3]$$

where the potential V_{hole} describes the walls initially present in the trap and where $\hat{H}$ is given by Eq. **1**. We denote the number of available sites before and after removing the walls by n^0_{sites} and n_{sites}, respectively, and we define the ratio $(1-\eta)=n^0_{\text{sites}}/n_{\text{sites}}$. When $V_{\text{hole}}=0$, the total number of sites within the trap is approximatively given by the area $n_{\text{site}}\approx\pi(r_0/a)^2$, while the outer circular edge contains about $n_{\text{edge}}\approx 2\pi r_0/a$ lattice sites. The holes in the density created by V_{hole} correspond to $n_{\text{hole}}=n_{\text{sites}}-n^0_{\text{sites}}\approx\pi(r_0/a)^2/\sqrt{2}$ vacant sites, leading to the large ratio $\eta=n_{\text{hole}}/n_{\text{sites}}\approx 1/\sqrt{2}$. For $r_0=27a$, the system initially contains $n^0_{\text{site}}\approx 700$ sites and the number of sites delimiting the edge of the bat is $n^0_{\text{edge}}\approx 320$ sites. Thus, the spacious holes used in our calculations lead to a large edge/bulk ratio. For $\Phi\approx p/q\in\mathbb{Q}$, and initially setting the Fermi energy in the lowest bulk gap, leads to the filling factor $\nu^0=N_{\text{part}}/n^0_{\text{sites}}\sim 1/q$. After removing the walls V_{hole}, the filling factor is reduced to the smaller value $\nu=N_{\text{part}}/n_{\text{sites}}\sim(1-\eta)/q\ll\nu^0$.

The groundstate of Hamiltonian Eq. **3** is written as

$$|\Psi_0\rangle=\prod_{E_\alpha<E_F}\hat{f}^\dagger_\alpha|\emptyset\rangle, \qquad [4]$$

where the operator $\hat{f}^\dagger_\alpha$ creates a particle in the single-particle state $|\chi_\alpha\rangle$, with energy E_α located below the Fermi energy E_F. Here $\{|\chi_\alpha\rangle,E_\alpha\}$ represents the complete set of single-particle eigenstates and eigenvalues satisfying the stationary Schrödinger equation

$$\hat{H}_0|\chi_\alpha\rangle=E_\alpha|\chi_\alpha\rangle. \qquad [5]$$

We are interested in the time evolution of the spatial density $\rho(\boldsymbol{x},t)$ after removing the walls V_{hole} at $t=0$. The evolution of the single-particle states $|\chi_\alpha\rangle$ is then entirely governed by the Hamiltonian $\hat{H}$. It is therefore convenient to introduce the eigenstates and eigenvalues $\{|\phi_\lambda\rangle,\epsilon_\lambda\}$ corresponding to the Hamiltonian $\hat{H}$,

$$\hat{H}|\phi_\lambda\rangle=\epsilon_\lambda|\phi_\lambda\rangle. \qquad [6]$$

We then define $|\chi_\alpha(t)\rangle$ as the time evolution of the initial state $|\chi_\alpha\rangle$ according to the Hamiltonian $\hat{H}$,

$$|\chi_\alpha(t)\rangle=\sum_\lambda\langle\phi_\lambda|\chi_\alpha\rangle e^{-i\epsilon_\lambda t/\hbar}|\phi_\lambda\rangle. \qquad [7]$$

The spatial density $\rho(\boldsymbol{x},t)$ at time t is given by

$$\rho(\boldsymbol{x},t)=\sum_{E_\alpha<E_F}|\chi_\alpha(\boldsymbol{x},t)|^2, \qquad [8]$$

namely, the particle density $\rho(\boldsymbol{x},t)$ is entirely governed by the time-evolution of the initially occupied single-particle states. The time evolution of the atomic cloud, after releasing the walls V_{hole} at $t=0$, can therefore be numerically evaluated through a direct diagonalization of the Hamiltonians $\hat{H}$ and $\hat{H}_0$. In our study, a crucial aspect consists in identifying the regimes for which the edge states propagating around the initially forbidden regions provide a clear signal, which is not perturbed by the many bulk states. It is therefore desirable to separately evaluate the contributions of the initially populated bulk and edge states. We introduce the corresponding quantities

$$\rho_{\text{edge}}(\boldsymbol{x},t)=\sum_{E_e<E_F}|\chi_e(\boldsymbol{x},t)|^2,$$

$$\rho_{\text{bulk}}(\boldsymbol{x},t)=\rho(\boldsymbol{x},t)-\rho_{\text{edge}}(\boldsymbol{x},t),$$

where the sum $\sum_{E_e<E_F}$ is restrained to the populated edge states with energies E_e located within the bulk gap.

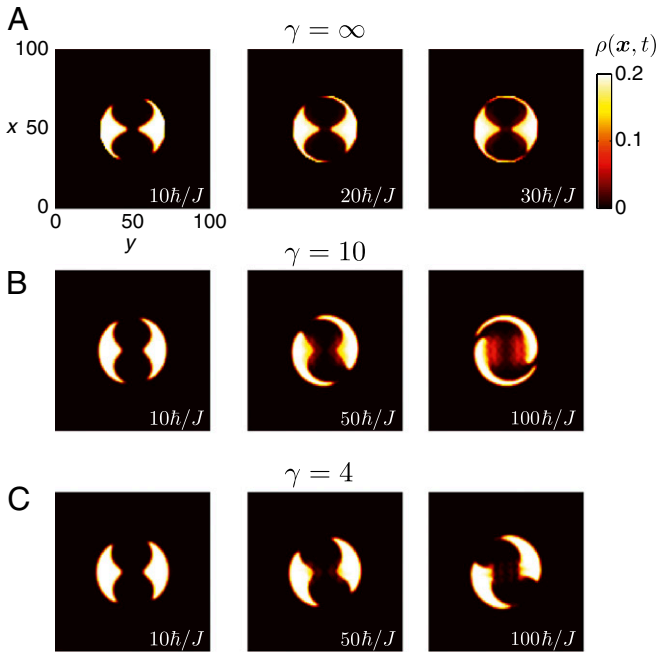

Fig. 8. Smooth confinements and the density evolution. Evolution of the spatial density for $\Phi=1/5$ and $E_F=-1.5J$. The walls V_{hole} are produced by asymmetric Gaussian potentials, with standard deviations $\sigma_y\approx\sqrt{2}\sigma_x$. The external confining potential is $V_{\text{conf}}(r)=V_0(r/r_0)^\gamma$, with $r_0=21a$ and $V_0=J$. (*A*) $\gamma=\infty$, (*B*) $\gamma=10$, and (*C*) $\gamma=4$. Note the broadening δr of the edge-state signal (Fig. 7) and also the deceleration of the motion as the confinement becomes smoother $\gamma=\infty\to 4$.

ACKNOWLEDGMENTS. We thank J. Beugnon, I. Bloch, G. Bulnes Cuetara, M. Müller, and S. Nascimbène for discussions. This work was supported by the Fonds de la Recherche Scientifique (FNRS Belgium), Agence Nationale de la Recherche (ANR) via the project AGAFON (Artificial gauge fields on neutral

atoms), European Research Council (ERC) project Quantum Gauge Theories and Ultracold Atoms (QUAGATUA), the Emergences program (Ville de Paris and Université Pierre et Marie Curie), and ERC Many-Body physics in gauge fields with ultracold Yb atoms in optical lattices (ManyBo) Starting Grant. Work at Innsbruck is supported by the integrated project AQUTE, the Austrian Science Fund through Spezialforschungsbereich (SFB) F40 FOQUS, and by the Defense Advanced Research Projects Agency (DARPA) Optical Lattice Emulator (OLE) program. I.B.S. acknowledges the financial support of the National Science Foundation (NSF) through the Physics Frontier Center at Joint Quantum Institute (JQI) and the Army Research Office (ARO) with funds from both the Atomtronics Multidisciplinary University Research Initiative (MURI) and DARPA OLE Program.

1. Hasan MZ, Kane CL (2010) Colloquium: Topological insulators. *Rev Mod Phys* 82: 3045–3067.
2. Qi XL, Zhang SC (2011) Topological insulators and superconductors. *Rev Mod Phys* 83: 1057–1110.
3. Thouless DJ, Kohmoto M, Nightingale MP, den Nijs M (1982) Quantized Hall conductance in a two-dimensional periodic potential. *Phys Rev Lett* 49:405–408.
4. Kohmoto M (1989) Zero modes and the quantized Hall conductance of the two-dimensional lattice in a magnetic field. *Phys Rev B Condens Matter* 39(16):11943–11949.
5. Hatsugai Y (1993) Chern number and edge states in the integer quantum Hall effect. *Phys Rev Lett* 71(22):3697–3700.
6. Ashoori RC, Stormer HL, Pfeiffer LN, Baldwin KW, West K (1992) Edge magneto-plasmons in the time domain. *Phys Rev B Condens Matter* 45(7):3894–3897.
7. Ji Y, et al. (2003) An electronic Mach-Zehnder interferometer. *Nature* 422(6930):415–418.
8. Zhang Y, et al. (2009) Distinct signatures for Coulomb blockade and Aharonov-Bohm interference in electronic Fabry-Perot interferometers. *Phys Rev B* 79:241304–241308.
9. Aidelsburger M, et al. (2011) Experimental realization of strong effective magnetic fields in an optical lattice. *Phys Rev Lett* 107(25):255301–255305.
10. Dalibard J, Gerbier F, Juzeliūnas G, Öhberg P (2011) Colloquium: Artificial gauge potentials for neutral atoms. *Rev Mod Phys* 83:1523–1543.
11. Brantut JP, Meineke J, Stadler D, Krinner S, Esslinger T (2012) Conduction of ultracold fermions through a mesoscopic channel. *Science* 337(6098):1069–1071.
12. Alba E, Fernandez-Gonzalvo X, Mur-Petit J, Pachos JK, Garcia-Ripoll JJ (2011) Seeing topological order in time-of-flight measurements. *Phys Rev Lett* 107(23):235301–235305.
13. Zhao E, Bray-Ali N, Williams C, Spielman IB, Satija I (2011) Chern numbers hiding in time-of-flight images. *Phys Rev A* 84:063629–063633.
14. Goldman N, et al. (2013) Measuring topology in a laser-coupled honeycomb lattice: From Chern insulators to topological semi-metals. *New J Phys*, 15:013025.
15. Price HM, Cooper NR (2012) Mapping the Berry curvature from semiclassical dynamics in optical lattices. *Phys Rev A* 85:033620.
16. Umucalilar RO, Zhai H, Oktel MÖ (2008) Trapped Fermi gases in rotating optical lattices: Realization and detection of the topological hofstadter insulator. *Phys Rev Lett* 100(7):070402–070405.
17. Scarola VW, Das Sarma S (2007) Edge transport in 2D cold atom optical lattices. *Phys Rev Lett* 98(21):210403–210406.
18. Goldman N, et al. (2010) Realistic time-reversal invariant topological insulators with neutral atoms. *Phys Rev Lett* 105(25):255302.
19. Stanescu TD, Galitski V, Das Sarma S (2010) Topological states in two-dimensional optical lattices. *Phys Rev A* 82:013608.
20. Goldman N, Beugnon J, Gerbier F (2012) Detecting chiral edge states in the Hofstadter optical lattice. *Phys Rev Lett* 108(25):255303–255305.
21. Kraus CV, Diehl S, Zoller P, Baranov MA (2012) Preparing and probing atomic Majorana fermions and topological order in optical lattices. *New J Phys* 14:113036–113052.
22. Killi M, Paramekanti A (2012) Use of quantum quenches to probe the equilibrium current patterns of ultracold atoms in an optical lattice. *Phys Rev A* 85:061606–061610.
23. Papp SB, et al. (2008) Bragg spectroscopy of a strongly interacting 85Rb Bose-Einstein condensate. *Phys Rev Lett* 101(13):135301–135304.
24. Goldman N, Beugnon J, Gerbier F (2013) Identifying topological edge states in 2D optical lattices using light scattering. *Eur Phys J Special Topics* 217:135–152.
25. Jaksch D, Zoller P (2003) Creation of effective magnetic fields in optical lattices: The Hofstadter butterfly for cold neutral atoms. *New J Phys* 5:56.
26. Gerbier F, Dalibard J (2010) Gauge fields for ultracold atoms in optical superlattices. *New J Phys* 12:033007.
27. Meyrath TP, Schreck F, Hanssen JL, Chuu CS, Raizen MG (2005) Bose-Einstein condensate in a box. *Phys Rev A* 71:041604–041607.
28. Weitenberg C, et al. (2011) Single-spin addressing in an atomic Mott insulator. *Nature* 471(7338):319–324.
29. Hofstadter DR (1976) Energy levels and wave functions of Bloch electrons in rational and irrational magnetic fields. *Phys Rev B* 14:2239–2249.
30. Buchhold M, Cocks D, Hofstetter W (2012) Effects of smooth boundaries on topological edge modes in optical lattices. *Phys Rev A* 85:63614–63625.
31. Sanchez-Palencia L, Lewenstein M (2010) Disordered quantum gases under control. *Nat Phys* 6:87–95.
32. Sørensen AS, Demler E, Lukin MD (2005) Fractional quantum Hall states of atoms in optical lattices. *Phys Rev Lett* 94(8):086803–086806.
33. Cooper NR (2008) Rapidly rotating atomic gases. *Adv Phys* 57:539–616.
34. Graß T, Juliá-Díaz B, Lewenstein M (2012) Quasihole dynamics as a detection tool for quantum Hall phases. *Phys Rev A* 86:053629–053635.
35. Béri B, Cooper NR (2011) Z(2) topological insulators in ultracold atomic gases. *Phys Rev Lett* 107(14):145301–145305.
36. Bermudez A, et al. (2010) Wilson fermions and axion electrodynamics in optical lattices. *Phys Rev Lett* 105(19):190404–190407.